Title

Cyclo[18]carbon including zero-point motion: ground state, first singlet and triplet excitations, and hole transfer.

Journal

Physical chemistry chemical physics : PCCP, 24(13)

ISSN

1463-9076

Authors

Lambropoulos, Konstantinos
Alvertis, Antonios M
Morphis, Andreas
et al.

Publication Date

2022-03-01

DOI

10.1039/d2cp00343k

Peer reviewed

PCCP

ARTICLE TYPE

Cite this: DOI: 00.0000/xxxxxxxxxx

Cyclo[18]carbon including Zero-Point Motion: Ground State, First Singlet and Triplet Excitations, and Hole Transfer†

Konstantinos Lambropoulos,*[a] Antonios M. Alvertis,[b,c], Andreas Morphis[a] and Constantinos Simserides[a]

Received Date
Accepted Date

DOI: 00.0000/xxxxxxxxxx

Recent synthesis of cyclo[18]carbon has spurred increasing interest in carbon rings. We focus on a comparative inspection of ground and excited states, as well as of hole transfer properties of cumulenic and polyynic cyclo[18]carbon via Density Functional Theory (DFT), time-dependent DFT (TD-DFT) and real-time time-dependent DFT (RT-TDDFT). Zero-point vibrations are also accounted for, using a Monte Carlo sampling technique and a less exact, yet mode-resolved, quadratic approximation. The inclusion of zero-point vibrations leads to a red-shift on the HOMO-LUMO gap and the first singlet and triplet excitation energies of both conformations, correcting the values of the 'static' configurations by 9% to 24%. Next, we oxidize the molecule, creating a hole at one carbon atom. Hole transfer along polyynic cyclo[18]carbon is decreased in magnitude compared to its cumulenic counterpart and lacks the symmetric features the latter displays. Contributions by each mode to energy changes and hole transfer between diametrically opposed atoms vary, with specific bond-stretching modes being dominant.

1 Introduction

More than half a century since the first report on the possibility to stabilize specific carbon rings with $n = 4q + 2$ $(q \geq 2)$ atoms[1], and 30 years after the first evidence for the generation of cyclo[18]carbon in gas phase[2], its synthesis, stabilization, and characterization was achieved in 2019[3], adding it to the family of experimentally relevant carbon allotropes. This development has drawn significant scientific attention to the study of cyclo[18]carbon. Its electronic structure[4–8], mechanical properties[9], intermolecular interactions[10,11], reaction mechanisms[12], doped structures[13,14] and analogues[15,16] are currently subjects of extensive research, aiming to understand its characteristics and potential applications. Our goal is to contribute to these efforts, by performing a comparative study on the –experimentally observed– polyynic conformation of cyclo[18]carbon and its more symmetric –albeit elusive, based on current knowledge– cumulenic counterpart, including zero-point motion.

In this work, we focus on the effect of zero-point vibrations on the ground state (using Density Functional Theory, DFT), first singlet and triplet excitation energies (using time-dependent DFT, TDDFT), and hole transfer properties (using real-time TDDFT, RT-TDDFT) of cumulenic and polyynic cyclo[18]carbon. Vibrations are taken into account using two methods. The first one is a Monte Carlo sampling technique. Some of the first descriptions of such a formalism can be found in the early works by Williams and Lax[17,18], who showed that one can make a semi-classical approximation by assuming vertical transitions between electronic states to accurately sample vibrational averages of the dielectric function of a system. Within our treatment, zero-point vibrations are taken into account using the Bose-Einstein distribution. This goes beyond the introduction of a thermal broadening or classical Molecular Dynamics simulations, which can be employed to get a classical approximation of the density of the initial vibrational states[19]. The second one is a less exact, yet mode-resolved, method, called below the quadratic method. This approach has been successfully applied recently to calculate the exciton energies of solid state organic semiconductors[20], and the Thiel[21] set of molecules plus anthracene, tetracene and pentacene[22], leading to improved agreement with experiment. Also, some of us have recently employed RT-TDDFT to study hole transfer in linear cumulenic and polyynic chains[23,24].

The rest of the paper is organized as follows: In Section 2,

[a] Department of Physics, National and Kapodistrian University of Athens, Panepistimiopolis, Zografos GR-15784, Athens, Greece. Email: klambro@phys.uoa.gr, amorphis@phys.uoa.gr, csimseri@phys.uoa.gr
[b] Cavendish Laboratory, University of Cambridge, J. J. Thomson Avenue, Cambridge CB3 0HE, United Kingdom. Email: ama80@cam.ac.uk
[c] Materials Sciences Division, Lawrence Berkeley National Laboratory, Berkeley, California 94720, USA

† Electronic Supplementary Information (ESI) available: Additional figures with details on DFT, TDDFT, and RT-DDFT results; video of hole transfer simulations. See DOI: 10.1039/cXCP00000x/.

we describe how we employ DFT, TDDFT and RT-TDDFT to study cumulenic and polyynic cyclo[18]carbon as well as and the methods used to account for zero-point motion. In Section 3, we present our results. Specifically, we discuss the ground states of the frozen, 'static', cumulenic and polyynic conformations as well as the effect of zero-point vibrations on the HOMO-LUMO gaps, first singlet and triplet excitation energies, and hole transfer along them. Finally, in Section 4 we state our conclusions. Additional figures and a video of RT-TDDFT simulations for hole transfer can be found in the Supporting Information.

2 Theory

2.1 DFT, TDDFT, RT-TDDFT

DFT[25,26] is among the most well-established and widely-used methods to investigate the ground state properties of many-body systems, e.g., molecules or solids. The ground state of the system is obtained by the self-consistent solution of the Kohn-Sham equations, which represent an assumed system of non-interacting electrons that produces the same density as the real system of interacting electrons. Two decades after its establishment, DFT was extended[27] to time dependent systems (TDDFT). Today, TDDFT is mainly applied to obtain the energies of excited states of molecules. The time-dependent Kohn-Sham (TDKS) equations with an effective potential energy $v_{\mathrm{KS}}(\vec{r},t)$, uniquely described by the time-dependent charge density, $\rho(r,t)$, are, in atomic units,

$$i\frac{\partial}{\partial t}\Psi_j(\vec{r},t) = \left[-\frac{1}{2}\nabla^2 + v_{\mathrm{KS}}(\vec{r},t)\right]\Psi_j(\vec{r},t), \tag{1}$$

where

$$v_{\mathrm{KS}}(\vec{r},t) = v_{\mathrm{ext}}(\vec{r},t) + v_{\mathrm{H}}(\vec{r},t) + v_{\mathrm{xc}}[\rho](\vec{r},t). \tag{2}$$

$v_{\mathrm{ext}}(\vec{r},t)$ includes the external fields and nuclear potentials, $v_{\mathrm{H}}(\vec{r},t)$ is the Hartree potential, and $v_{\mathrm{xc}}[\rho](\vec{r},t)$ includes the exchange and correlation effects. The total charge density of the system is

$$\rho(\vec{r},t) = \sum_{j=1}^{N_{\mathrm{occ}}} \left|\Psi_j(\vec{r},t)\right|^2, \tag{3}$$

i.e., the sum of the density of all occupied orbitals $j = 1,2,\ldots,N_{\mathrm{occ}}$. Within TDDFT, the system of equations (1) is commonly solved using the linear response method, which is not actually a time-resolved method; instead, it solves TDKS equations in the frequency domain to obtain the excitation energies of a system subject to a small perturbation. In contrast, RT-TDDFT[28] is based on a direct numerical integration of Eq (1). The TDKS equations are solved and the electron density is obtained at each time step. The density is then used to calculate the Hamiltonian in the next cycle of the self-consistent process. Our DFT, TDDFT, and RT-TDDFT calculations were performed using NWChem[29].

For our RT-TDDFT simulations of hole transfer, we initially performed a ground-state DFT calculation on the neutral molecule, found the charge at each atom via Löwdin population analysis[30], and then created the initial state with Constrained Density Functional Theory (CDFT), putting everywhere the previously obtained charges, apart from atom 1 [see Fig. 1(a) below], which was oxidized: Its charge was increased by +1, i.e., a hole was created. The charge constraints were obtained with Löwdin population analysis[30], which was also used in the subsequent RT-TDDFT simulation. Löwdin population analysis was integrated into the RT-TDDFT module of NWChem for the calculation of each fragment's charge at each time step. It is much less basis-set dependent and does not suffer from the ultrafast charge oscillations that Mulliken analysis (the default scheme in NWChem's RT-TDDFT implementation) artificially introduces in charge transfer simulations, thus giving a clearer picture of charge transfer. In a Gaussian basis set, it is most natural to use the single particle reduced density matrix, whose time evolution is governed by the von Neumann equation. The Magnus propagator is used in NWChem's RT-TDDFT implementation, which is both stable and conserves the density matrix idempotency[28]. At the end of each time step, the charge is calculated at each atom, along with the dipole moment. We used a time step of 0.5 a.u..

Our DFT, TDDFT, and RT-TDDFT calculations were carried out at the same level of theory. Specifically, we used the cc-pVTZ[31] basis-set, i.e., the smallest one for which vibrational analysis showed no imaginary frequencies for both cumulenic and polyynic cyclo[18]carbon. Basis sets 6-31G*[32,33] and cc-pVDZ[31] displayed two and one imaginary frequencies, respectively. This is a straightforward way to confirm the energy minimum, albeit, in principle, optimization of a true minimum can be achieved with any given basis set, e.g. by elongating the atomic positions along the coordinates of negative frequencies. Regarding the exchange-correlation functional, it has been established that the weight of the exact (Hartree-Fock, HF) exchange in the DFT functional determines the minimum energy structure predicted for cyclo[18]carbon: specifically, functionals with less amount of HF exchange lead to the cumulenic conformation, while larger amounts of HF exchange induce bond length alternation (BLA), thus leading to the polyynic conformation[4,8,34–36]. Thus, in order to be as consistent as possible in our comparison between the two structures, we recruited the popular B3LYP[37–40] functional, as follows: the B3LYP exchange-correlation energy is defined by a combination of HF, Slater (S), and Becke 1988[41] (B88) exchange terms, as well as Lee-Yang-Parr[38] (LYP) and Vosko-Wilk-Nusair[39] (VWN) correlation terms, using three parameters. Namely,

$$E_{\mathrm{xc}} = \alpha_0 E_{\mathrm{x}}^{\mathrm{HF}} + (1-\alpha_0)E_{\mathrm{x}}^{\mathrm{Slater}} + \alpha_{\mathrm{x}} E_{\mathrm{x}}^{\mathrm{B88}} + \alpha_{\mathrm{c}} E_{\mathrm{c}}^{\mathrm{LYP}} + (1-\alpha_{\mathrm{c}})E_{\mathrm{c}}^{\mathrm{VWN}}, \tag{4}$$

where $E_{\mathrm{x(c)}}^{\mathrm{T}}$ is the exchange (correlation) term T, and $\alpha_0 = 0.2$, $\alpha_{\mathrm{x}} = 0.72$, $\alpha_c = 0.81$. Using these values of the parameters, i.e., the original B3LYP with 20% exact exchange, we obtained a cumulenic structure, while, setting $\alpha_0 = 0.6$, i.e., 60% exact exchange, and leaving the rest parameters unchanged, we were led to a polyynic structure.

2.2 Inclusion of Vibrations

The contributions of the molecular vibrations of a system to a quantum mechanical observable at temperature T, $\hat{O}(T)$, can be expressed in terms of the standard quantum mechanical expectation value

$$O(T) = \frac{1}{Z}\sum_s \langle \chi_s(\vec{u})|\hat{O}(\vec{u})|\chi_s(\vec{u})\rangle\, e^{-\frac{E_s}{k_B T}}, \tag{5}$$

where $\vec{u}$ is the nuclear displacement vector, $|\chi_s(\vec{u})\rangle$ is a vibrational eigenstate on the ground state potential energy surface with energy E_s, $Z = \sum_s e^{-\frac{E_s}{k_B T}}$ is the partition function, and $\hat{O}(\vec{u})$ is the observable of interest once the system is displaced by $\vec{u}$. Within the harmonic approximation for the ground state potential, we can substitute $|\chi_s(\vec{u})\rangle$ with the wavefunctions of the quantum harmonic oscillator, thus obtaining [42]

$$O(T) = \int d\vec{u} |\Phi(\vec{u},T)|^2 O(\vec{u}). \quad (6)$$

$|\Phi(\vec{u},T)|^2$ is the harmonic density at temperature T, given by the expression

$$|\Phi(\vec{u},T)|^2 = \prod_\nu \frac{\exp\left(-\frac{u_\nu^2}{2\sigma_\nu^2(T)}\right)}{\sqrt{2\pi}\sigma_\nu(T)}, \quad (7)$$

where

$$\sigma_\nu^2(T) = \frac{1}{2\omega_\nu} \coth\left(\frac{\omega_\nu}{2k_B T}\right). \quad (8)$$

The index ν runs over the vibrational modes of the system, and ω_ν is the frequency of mode ν. Atomic units and mass-weighted coordinates have been used.

It is worth noting that the harmonic approximation to the molecular vibrations which was made above can lead to errors, particularly when studying molecular properties at room temperature, where highly anharmonic low-frequency modes can be strongly activated. Here, we focus on the case of 0 K, hence vibrations are only active with their zero-point energy $\frac{\hbar\omega}{2}$, so it is the harmonic high-frequency modes that dominate, and this is not generally an issue. The anharmonic effects that arise at room temperature can be captured by approaches such as classical molecular dynamics, however these would entirely miss the impact of nuclear quantum fluctuations, which is significant and even dominant for smaller molecules [20,22]. Ab initio molecular dynamics at finite temperatures have been implemented attempting to describe excited state properties [43], optical spectroscopy [44] and excited state dynamics [45], while, path integral molecular dynamics have been implemented attempting to describe nuclear quantum and anharmonic effects [46,47]. Finally, while our technique focuses on describing the effect of equilibrium nuclear configurations at a chosen temperature, excited state spectroscopy simulations have been implemented to provide information on the effect of vibrations that have been displaced due to electronic excitation [48], or even on peculiarly displaced vibrational configurations that can lead to non-adiabatic transitions [49,50].

The integral of Eq. (6) can by approximated using the Monte Carlo method by generating a sample of configurations $\vec{u}$, according to the harmonic distribution at a specific temperature T, so that the expectation value of the observable $O(T)$ can be computed as a simple average of the sample values. This method relies on no adjustable parameters, apart from the choice of DFT functional and basis set, which are fixed throughout the entire series of calculations. Alternative methods have been proposed in the past, such as the nuclear ensemble approach used within the quantum chemistry community [51,52] or methods that generate initial nuclear configurations from a Boltzmann distribution to sample vibrational averages of observables [53,54], although the latter would not capture the effects of zero-point motion.

In practice, in order to sample the integral of Eq. (6), we generate 100 displaced configurations for both cumulenic and polyynic cyclo[18]carbon at $T = 0$ K and obtain the renormalized HOMO-LUMO gaps (using DFT), first singlet (S_1) and first triplet (T_1) excitation energies (using TDDFT within the Tamm-Dancoff approximation [55]), as well as quantities related to hole transfer (using RT-TDDFT), versus those of their 'static', frozen, conformations.

Eq. (6) can be simplified by expanding the observable $O(\vec{u})$ in the vibrational coordinates $\vec{u}$ as

$$O(\vec{u}) = O(\vec{0}) + \sum_\nu \frac{\partial O(\vec{0})}{\partial u_\nu} u_\nu + \frac{1}{2}\sum_\nu\sum_{\nu'} \frac{\partial^2 O(\vec{0})}{\partial u_\nu \partial u_{\nu'}} u_\nu u_{\nu'} + \ldots, \quad (9)$$

yielding

$$O(T) \approx O_{\text{static}} + \sum_\nu \frac{1}{2\omega_\nu} \frac{\partial^2 O(\vec{u})}{\partial u_\nu^2} \left[\frac{1}{2} + n_{BE}(\omega_\nu, T)\right] + \mathcal{O}(u_\nu^4). \quad (10)$$

$O_{\text{static}} = O(\vec{0})$ is the value of the observable in the static geometry and $n_{BE}(\omega_\nu, T)$ is the Bose-Einstein distribution of the vibrational quanta. The odd terms vanish, since $|\Phi(\vec{u},T)|^2$ is a product of even, Gaussian, functions. Hence, this quadratic approximation is fourth-order accurate in $\vec{u}$. We have used Eq. (10) in our calculations, estimating the second derivative involved with the finite difference formula

$$\frac{\partial^2 O(\vec{u})}{\partial u_\nu^2} = \frac{O(\delta u_\nu) + O(-\delta u_\nu) - 2O_{\text{static}}}{\delta u_\nu^2}. \quad (11)$$

Hence, apart from the static value, two values of the observable are needed for each mode at displacements $\pm\delta u_\nu$, resulting in a total of $2(3N-6)+1$ calculations, where N is the number of atoms. Although, in principle, δu_ν is an infinitesimal quantity, in practice, a finite value needs to be chosen to avoid numerical divergence issues. In our case of cyclo[18]carbon, the computational cost of the quadratic approximation is comparable to the Monte Carlo method described above (a comparison of the two methods in terms of computational cost can be found in Ref. [22]). Although the quadratic method is less accurate than the Monte Carlo method, since it involves an expansion of the observable and a finite-difference estimation of its second derivative, it has a significant advantage: in Eq. (10), the correction to the observable is expressed as a sum over the vibrational modes, the contribution of each of which can be isolated, allowing for additional microscopic insights. Moreover, it has been shown for the specific case of computing excited state energies at a temperature T, the quadratic approximation may be written in the equivalent form [22,56]

$$E(T) = E_{\text{static}} - \frac{1}{4}\sum_\nu \frac{\omega_\nu^2 - \omega_{E\nu}^2}{\omega_\nu} [\frac{1}{2} + n_B(\omega_\nu, T)] + \mathcal{O}(u_\nu^4), \quad (12)$$

where $\omega_{E\nu}$ denotes the frequency of vibrational mode ν on the excited state. In organic molecules, the excited state surface generally has a smaller curvature than the ground state one, due to contributions from anti-bonding molecular orbitals, giving $\omega_\nu > \omega_{E\nu}$ in most cases. This in turn means that molecular vibrations will lead to a *red-shift* of excited state energies and HOMO-LUMO gaps

in these systems, apart from perhaps limited special cases. As seen in our Results section, this intuitive picture is validated by our first-principles Monte Carlo sampling in every case.

3 Results

3.1 Ground States of Static Conformations

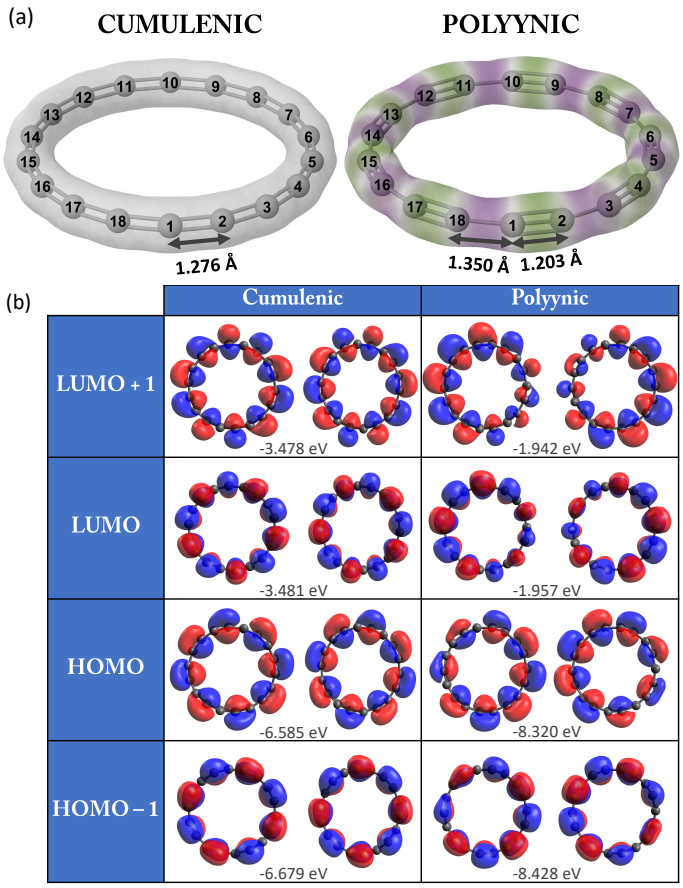

Fig. 1 Ground-state details of cyclo[18]carbon. (a) Structure and charge density for the cumulenic (left) and polyynic (right) case, optimized using the functional of Eq. (4) with $\alpha_0 = 0.2$ and $\alpha_0 = 0.6$, respectively, and the cc-pVTZ basis-set. The colors in the polyynic case correspond to regions where its density is larger (green) or smaller (purple) than the cumulenic one. (b) Shape and energy of the frontier orbitals from HOMO -1 to LUMO $+1$.

Starting from a carbon ring of 18 atoms in a cumulenic conformation with bond length 1.282 Å as an initial guess, we optimized the geometry using the functional of Eq. (4), for $\alpha_0 = 0.2$ (the default B3LYP value) and $\alpha_0 = 0.6$, and the cc-pVTZ basis set, without symmetry constraints, arriving at cumulenic and polyynic conformations, respectively. We have also checked (for $\alpha_0 = 0.2$, which is possible within NWChem) that the inclusion of D3 dispersion corrections[57] did not produce any significant changes to the properties studied in this work. Our results are summarized in Fig. 1. The cumulenic structure ($\alpha_0 = 0.2$) belongs to the D_{18h} point group with a bond length of 1.276 Å (BLA $= 0$ Å), while the polyynic structure belongs to the D_{9h} point group with alternating bond lengths of 1.203 Å and 1.350 Å (BLA $= 0.147$ Å). The BLA of the latter conformation is in very good agreement with the reported values for higher levels of theory (0.1447 Å within CCSD/cc-pVDZ[58] and 0.147 Å within DLPNO-CCSD(T)/Def2-TZVP[8]). The ground-state density of the cumulenic configuration has a toroidal shape; on the contrary, the polyynic case exhibits density maxima (minima) in the middle of the distance between short (long) bonds. In Fig. 1(a), the green (purple)-colored regions of the polyynic density show where it is larger (smaller) than the cumulenic one. Vibrational analysis confirming the minimum of energy in each case is provided in Fig. S1. The frontier orbitals of both structures, namely HOMO-1, HOMO, LUMO, LUMO$+1$, all of which have a π character, are presented in Fig. 1(b), together with their energies. These orbitals are doubly degenerate, have 8, 8, 10, and 10 nodes, and are out-of-plane, in-plane, out-of-plane, and in-plane, respectively. In the cumulenic case (left column), for HOMO-1 (-6.679 eV) and HOMO (-6.585 eV), a C_2 rotation leaves the orbitals unchanged, while an additional phase-flip is needed for LUMO (-3.481 eV) and LUMO$+1$ (-3.478 eV). In the polyynic case (right column), for each of the HOMO-1 (-8.428 eV), HOMO (-8.320 eV), LUMO (-1.957 eV), LUMO$+1$ (-1.942 eV) orbitals, there is one reflection plane plus a phase-flip or just one reflection plane that leaves the orbitals unchanged. We note that differences in the symmetry of the frontier orbitals have been described as consequence of spontaneous symmetry breaking, driven by the second order Jahn-Teller effect, which leads to the stabilization of the polyynic structure[7]. Additional orbital energies for both cases are provided in Fig. S2.

3.2 HOMO-LUMO gaps as well as first singlet and triplet excitation energies, including zero-point vibrations

In Fig. 2(a)-(c) we present the HOMO-LUMO gaps, obtained via DFT, as well as the first singlet (S_1) and triplet (T_1) excitation energies, obtained via TDDFT, of cumulenic and polyynic cyclo[18]carbon, comparing their static values with the renormalized ones due to zero-point vibrations, using the Monte Carlo method. Further results and details on the sample-convergence of these values can be found in Figs. S3–S4. As expected, the cumulenic conformation has a smaller HOMO-LUMO gap than the polyynic one. Additionally, in both cases, the lowest excitation energy corresponds to a triplet state, while for both T_1 and S_1 the excitation energy is lower in the cumulenic conformation. Furthermore, it is clear that the inclusion of zero-point motion leads to a reduction of the static values in all cases, to an extent ranging from $\approx 9\%$ to $\approx 24\%$ of the static values. This reduction (red-shift) of excitation energies can be explained through the difference between the curvatures of the potential energy surface of the ground and excited states (see Eq. (12) and the relevant discussion), and is in accordance with the recent attribution of the red-shift in the absorption maxima of molecules compared to their, 'static', vertical excitation energies to contributions from the vibrational modes, using the nuclear ensemble method combined with CCSD calculations[52]. Of course, an accurate and complete description of absorption spectra in their entirety would require the inclusion of Franck-Condon progression[59].

The contribution of each vibrational mode to the renormal-

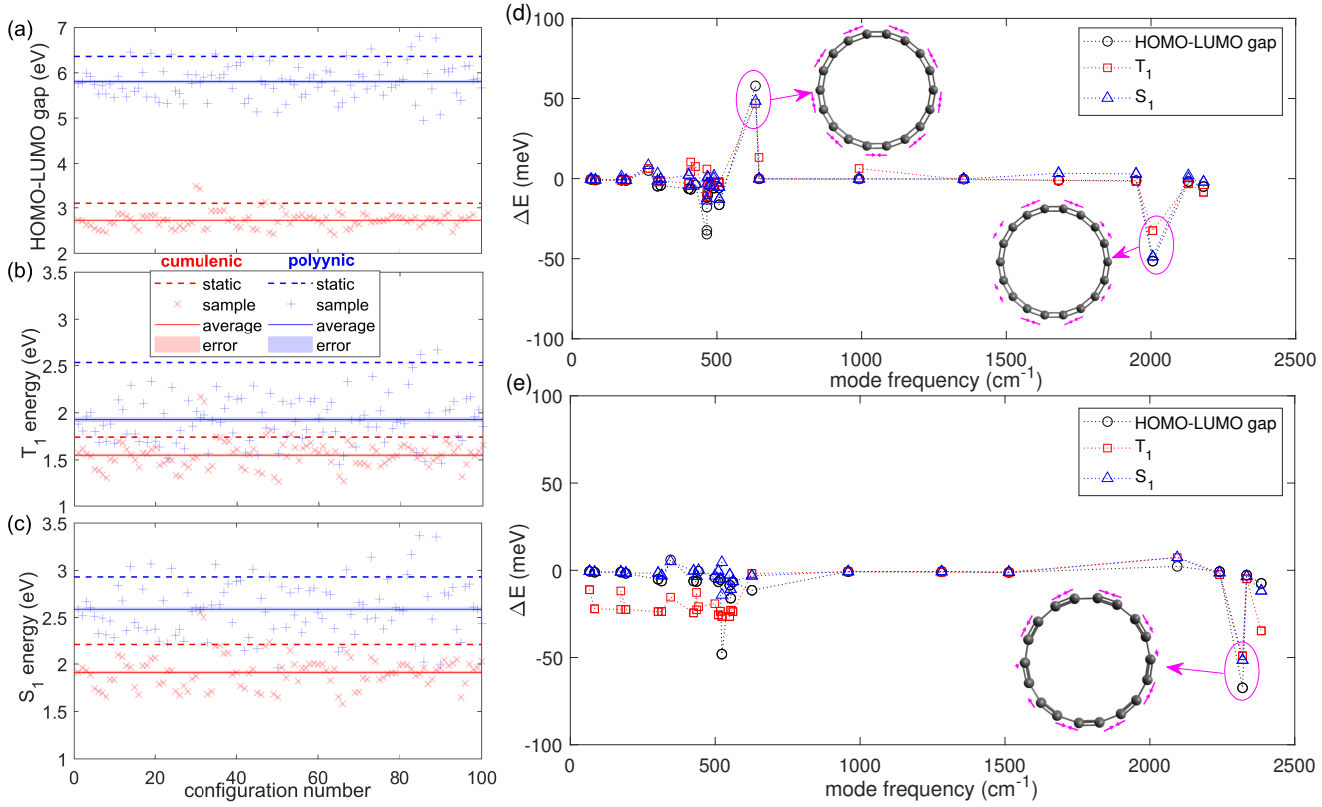

Fig. 2 (a) HOMO-LUMO gap, (b) T_1 excitation energy, and (c) S_1 excitation energy of static cumulenic and polyynic cyclo[18]carbon, compared with their corresponding renormalized values due to zero-point motion, using the Monte Carlo method. The values for each Monte Carlo sample are also shown. (d) Contribution of each vibrational mode to the energy correction of the HOMO-LUMO gap (circles), T_1 excitation (squares), and S_1 excitation (triangles) of cumulenic cyclo[18]carbon due to vibrations within the quadratic method. The displacement patterns of the modes with major contribution to the overall renormalization values are also shown. Dotted lines are just guides to the eye. (e) Same as (d), for polyynic cyclo[18]carbon.

Table 1 Comparison of the 'static' and renormalized (due to zero-point motion using the quadratic and Monte Carlo methods) values, of the HOMO-LUMO gaps as well as of the T_1 and S_1 excitation energies of cumulenic and polyynic cyclo[18]carbon. All values are given in eV. Standard errors are shown in parentheses.

Cumulenic	LUMO-HOMO	T_1	S_1
Static	3.104	1.742	2.215
Quadratic	2.819	1.678	2.101
Monte Carlo	2.728(18)	1.551(15)	1.911(17)
Polyynic	LUMO-HOMO	T_1	S_1
Static	6.363	2.533	2.930
Quadratic	5.942	1.671	2.706
Monte Carlo	5.805(37)	1.927(25)	2.588(29)

ization of the 'static' values, obtained by the quadratic method, is shown in Fig. 2(d)-(e). This method, albeit less exact due to its approximate character and the finite difference approach undertaken (a displacement step of $\delta u_\nu = 4\sigma_\nu$ was needed to start reaching convergence), follows the trend of the Monte Carlo method in terms of differences from the static values (see Table 1, where we present a comparison between the energies of the HOMO-LUMO gap, T_1, and S_1 for the static cases versus the ones obtained via the quadratic and Monte Carlo methods). In both conformations, there is one (doubly degenerate) mode with a major contribution towards the overall reduction of the 'static' values for the HOMO-LUMO gaps, and T_1 and S_1 excitations (in the T_1 excitation of the polyynic case, there are also several low-frequency modes that contribute rather significantly). This is a bond stretching mode, at ≈ 2004 cm^{-1} for the cumulenic conformation and at ≈ 2317 cm^{-1} for the polyynic one. Additionally, in all calculations for the cumulenic case, there is another bond-stretching mode, at ≈ 638 cm^{-1}, which contributes to the other end, i.e., towards an increase of the static value. This can be explained through the displacement pattern of this specific mode, that, at each snapshot, leads to a D_{9h}–symmetric, polyynic configuration, for which all values in Table 1 are larger compared to the respective ones for the cumulenic configuration. In other words, this mode tends to shift the cumulenic HOMO-LUMO gap and S_1 and T_1 energies towards the polyynic ones. Using HF-rich functionals (BMK, M06-2X, BHandHLYP and wB97XD, which stabilize the polyynic conformation), a mode of the cumulenic conformation with the same displacement pattern has been found to correspond to an imaginary frequency, hinting that the cumulenic conformation is a transition state between two polyynic conformations with inverted bond lengths[4]. We have checked that the displacement pattern of this mode [shown in Fig. 2(d)] is the same as the one discussed in Ref.[4] by performing calculations at the M06-2X/6-311++G** level (as in Ref.[4]) using the Nudged Elastic Band method[60–63] to find the minumum energy path between two polyynic conformations with inverted bond lengths, and a subsequent saddle point optimization and vibrational anal-

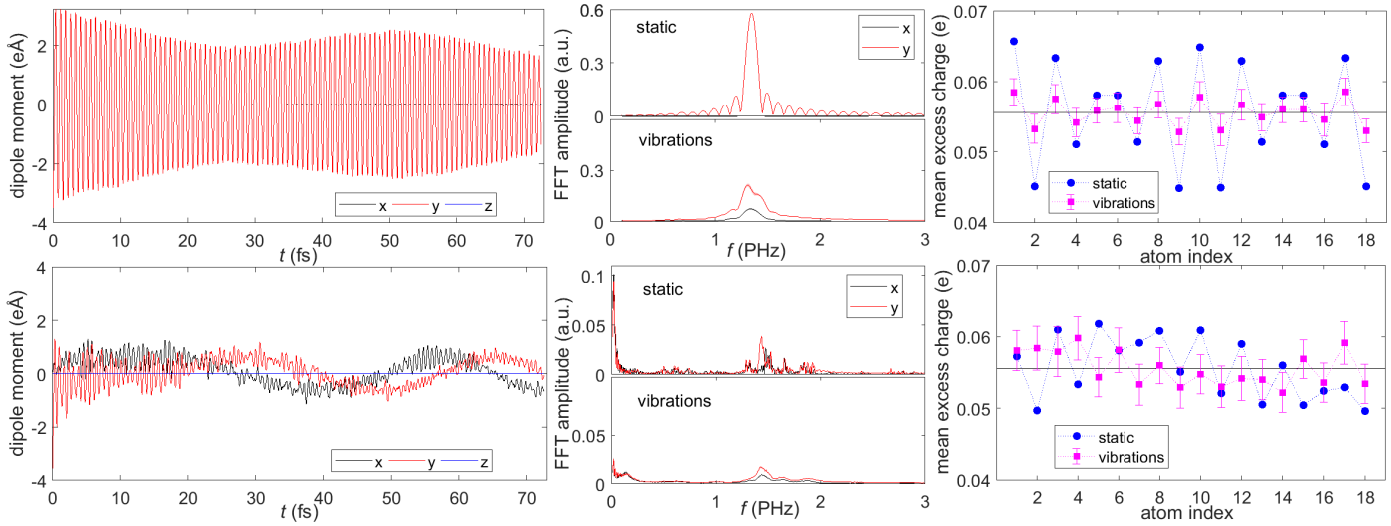

Fig. 3 Hole transfer in cumulenic (first row) and polyynic (second row) cyclo[18]carbon. (Left column) Time evolution of the dipole moment of the static configuration. (Middle column) FFT spectra of the dipole moment of the static configuration and averaged FFT spectra of the Monte Carlo sample (with standard errors, not visible in this scale), accounting for molecular vibrations. (Right column) Mean excess charge distribution at each atom for the static configuration versus the averaged mean excess charge distribution of the Monte Carlo sample (with standard errors), accounting for molecular vibrations. Dotted lines are guide for the eye.

ysis of the resulting intermediate cumulenic structure. Hence, although within our treatment the cumulenic configuration is a minimum energy structure as is the polyynic one, the quadratic method catches the tendency of the former to shift towards the latter.

3.3 Oxidation and subsequent hole transfer

For our RT-TDDFT simulations for hole transfer, the cyclo[18]carbon molecules are placed in the xy-plane, so that two diametrically opposed C atoms [atoms 1 and 10, cf. Fig 1(a)] lie on the y axis. We oxidize atom 1, i.e., we create a hole on atom 1, and examine its time-evolution. For the 'static' configurations, the simulation was carried out for ≈ 72.6 fs (i.e., 3000 a.u.) and the time-convergence of the time-averaged excess charge distribution was checked to obtain the maximum simulation time for the Monte Carlo sample (in the cumulenic case we found that 400 a.u. were adequate, while in the polyynic case 3000 a.u. were needed; cf. Fig. S5). The main results of our RT-TDDFT simulations for hole transfer are summarized in Fig. 3 and in Table 2.

Table 2 Comparison of 'static' and renormalized (due to zero-point motion using the Monte Carlo method) values of the maximum value of excess charge, p, at the atom diametrically opposed to the one the hole was initially placed, and the pure mean transfer rate, k. Standard errors are shown in parentheses.

	p (e)		k (PHz)	
	cumulenic	polyynic	cumulenic	polyynic
Static	0.2753	0.1516	0.2546	0.2212
Monte Carlo	0.2142(34)	0.1320(27)	0.2300(86)	0.2010(77)

Let us first comment on Fig. 3. As evident by comparing the panels in the left column, hole transfer is enhanced in the cumulenic case, while the waveforms of the time evolution of dipole moment are distinct between the two conformations. In the cumulenic case (first row of Fig. 3), deviations of the dipole moment in the static configuration occur solely on the y-axis, in the form of a fast oscillation (≈ 1.35 PHz, cf., the FFT spectrum in the top middle panel), since contributions on the x-axis cancel each other out due to the D_{18h} symmetry of the molecule. The inclusion of molecular vibrations has only a slight effect on the frequency content of the y-dipole moment oscillations; however, a weaker x-component with approximately the same frequency content is induced, due to distortions. Additionally, the time-averaged distribution of excess charge has a symmetric shape, with diametrically opposed atoms having the same amount of average excess charge. Moreover, atoms 1 (the atom at which the hole was initially placed) and 10 (its diametrically opposed one) possess the largest amount of excess charge, since the charge density initially located on atom 1 splits into two equivalent paths along the two semicircles defined by the y axis which interfere onto atom 10. Although the inclusion of molecular vibrations tends to shift the mean excess charge values towards 1/18 (i.e., towards equidistribution, cf., the horizontal line in the right column), the shape of the overall distribution remains the same. In the polyynic case (second row of Fig. 3), the situation is rather different. Deviations of the dipole moment in the static configuration occur on both the $x-$ and y-axes. The magnitude of the deviations is smaller and their frequency content is richer than in the cumulenic case, having one dominant peak in the THz regime (at ≈ 227 THz and 240 THz, for the x- and y- axis, respectively), and a secondary frequency band in the range ≈ 1.2 - 2 PHz (cf., the FFT spectra in the top middle panel). The inclusion of molecular vibrations has a significant effect on the frequency content of the x- and y- dipole moment oscillations; the dominant peak of the static case is reduced in intensity and widened into a sub-PHz frequency band, the FFT amplitude of which is now comparable to the one of the band at ≈ 1.2 - 2 PHz. Furthermore, in the static polyynic case, the time-averaged distribution of excess charge does not display any symmetry. Atom 10 gains, on average, a significant amount

of excess charge. It is clear that the path of the semicircle that starts with a short bond (i.e., from atom 1 to atom 2) is favored over the one that starts with a long bond (from atom 1 to atom 18). The inclusion of molecular vibrations significantly reduces the amount of excess charge at atom 10, while, although the aforementioned path starting with the short bond is still generally favored, the hole tends to be mostly distributed among atoms that lie closer to atom 1. We also note that the splitting of the charge into two equivalent paths (dominance of the path starting with short bonds) in the cumulenic (polyynic) case reported here has also been observed in the context of charge transport calculations on cyclo[18]carbon attached between atomic-carbon chain electrodes[64]. The above mentioned features are also demonstrated in the Supplementary Video. There we visualize the time evolution of the excess charge density for the first 92.5 au (2.23 fs) of our simulations. We compare both the static cumulenic and polyynic cases with relevant representative Monte Carlo configurations.

We focus now on charge transfer at the atom diametrically opposed to the one that the hole was initially placed (i.e., charge transfer from atom 1 to atom 10) by obtaining the maximum value of excess charge at atom 10, p, and the pure mean transfer rate, which is defined as $k = \frac{\langle C_{10}(t)\rangle}{t_{10mean}}$, where t_{10mean} is the time it takes for the excess charge at atom 10 to reach its mean value, $\langle C_{10}(t)\rangle$, for the first time. Our results are summarized in Table 2 (details on the sample-convergence of these values can be found in Fig S6).

Table 2 reaffirms that hole transfer between diametrically opposed atoms is enhanced in the cumulenic case, in terms of both p and k, while the inclusion of vibrations leads to a reduction of their values. The reduction of p is more significant in the cumulenic case, with its renormalized value due to vibrations being $\approx 22.2\%$ smaller than the static one, compared to an $\approx 12.9\%$ decrease in the polyynic case. On the contrary, k displays a less significant decrease, of $\approx 9.7\%$ and 9.1%, respectively. Finally, using the quadratic method, we checked whether the bond stretching modes that have major contributions to the zero-point corrections in the HOMO-LUMO gaps as well as the T_1 and S_1 energies (see above) remain significant for hole transfer in terms of p and k. To this end, for the cumulenic (polyynic) case, we focused on the mode at ≈ 2004 cm^{-1} (≈ 2317 cm^{-1}) and the mode at ≈ 1350 cm^{-1} (≈ 1280 cm^{-1}) which display major and minor contributions on the aforementioned properties, respectively [cf., Fig. 2(d)-(e)]. Indeed, the contributions of the former modes are much more significant than of the latter, contributing to the reduction of the absolute 'static' values from three times to three orders of magnitude more than the latter modes (cf. Fig. S7).

4 Conclusion

In summary, we comparatively studied the ground state, S_1 and T_1 excitations, and hole transfer properties of cumulenic and polyynic cyclo[18]carbon, focusing on the significant changes induced by zero-point motion. The Monte Carlo sampling technique accounting for zero-point corrections showed that the HOMO-LUMO gap and excitation energies are reduced in both cases. The contribution of vibrations amounts to at least 9% of the frozen, 'static' energy values, making them significant for more accurate predictions. The less exact, quadratic approximation, reveals that there are specific bond-stretching modes with very significant contributions towards changes in energy. While the zero-point renormalization of the HOMO-LUMO gap and excited state energies is inherent to a material, it would still be possible to probe it experimentally through the substitution of the carbon atoms of the studied system by heavier isotopes (e.g. Carbon-13, which is also stable). This would result to a reduction of the zero-point energy, $\frac{\hbar\omega}{2}$, of the vibrational modes, potentially leading to a substantial blue-shift of the excited state energies, something which has also been proposed in the case of metallic hydrogen[65]. Hole transfer in the cumulenic case is faster and displays enhanced and highly symmetric features which are preserved by the inclusion of vibrations, while, in the polyynic case, the semicircular path starting with the short bond is favored. Our treatment can be extended to study several additional properties of cyclo[18]carbon and other carbon rings and, of course, can also be recruited to the study of other relevant systems.

Author Contributions

Conceptualization: KL, AMA, CS. Data curation: KL. Formal analysis: KL, AMA, AM. Funding acquisition: CS. Investigation: KL, AMA, AM, CS. Methodology: KL, AMA, AM, CS. Project administration: CS. Resources: KL, AMA, AM, CS. Software: KL, AMA, AM. Supervision: CS. Validation: KL, AMA, CS. Visualization: KL. Writing - original draft: KL. Writing - review and editing: KL, AMA, AM, CS.

Conflicts of interest

There are no conflicts to declare.

Acknowledgements

This research is cofinanced by Greece and the European Union (European Social Fund - ESF) through the Operational Programme "Human Resources Development, Education and Lifelong Learning 2014-2020" in the context of the project "Charge transfer and transport in open and closed molecular wires made of carbon or carbon - nitrogen." (MIS 5047971). A.M.A. acknowledges the support of the Winton Programme for the Physics of Sustainability. This work was partially supported by computational time granted from the Greek Research and Technology Network (GRNET) in the National HPC facility (ARIS) under Project ID pr009028_thin (MONanoBio).

References

1 R. Hoffmann, *Tetrahedron*, 1966, **22**, 521–538.
2 F. Diederich, Y. Rubin, C. B. Knobler, R. L. Whetten, K. E. Schriver, K. N. Houk and Y. Li, *Science*, 1989, **245**, 1088–1090.
3 K. Kaiser, L. M. Scriven, F. Schulz, P. Gawel, L. Gross and H. L. Anderson, *Science*, 2019, **365**, 1299–1301.
4 G. V. Baryshnikov, R. R. Valiev, A. V. Kuklin, D. Sundholm and H. Ågren, *J. Phys. Chem. Lett.*, 2019, **10**, 6701–6705.
5 Z. Liu, T. Lu and Q. Chen, *Carbon*, 2020, **165**, 461–467.
6 B. Shi, L. Yuan, T. Tang, Y. Yuan and Y. Tang, *Chem. Phys. Lett.*, 2020, **741**, 136975.

7 Z. S. Pereira and E. Z. da Silva, *J. Phys. Chem. A*, 2020, **124**, 1152–1157.

8 A. J. Stasyuk, O. A. Stasyuk, M. Solà and A. A. Voityuk, *Chem. Commun.*, 2020, **56**, 352–355.

9 S. Fang and Y. H. Hu, *Carbon*, 2021, **171**, 96–103.

10 Z. Liu, T. Lu and Q. Chen, *Carbon*, 2021, **171**, 514–523.

11 J. L. Chen and R. Q. Zhang, *Adv. Theory Simul.*, 2021, **4**, 2100022.

12 J. Chen, L. Sun and R. Zhang, *Phys. Chem. Chem. Phys.*, 2021, **23**, 17545–17552.

13 X. Hou, Y. Ren, F. Fu and X. Tian, *Comput. Theor. Chem.*, 2020, **1187**, 112922.

14 Y. Ling, Q. L. Lu and Q. Q. Luo, *Eur. Phys. J. D*, 2021, **75**, 229.

15 F. Pichierri, *Chem. Phys. Lett.*, 2020, **738**, 136860.

16 A. E. Raeber and D. A. Mazziotti, *Phys. Chem. Chem. Phys.*, 2020, **22**, 23998–24003.

17 F. E. Williams, *Phys. Rev.*, 1951, **82**, 281–282.

18 M. Lax, *J. Chem. Phys.*, 1952, **20**, 1752–1760.

19 A. Petrone, J. Cerezo, F. J. A. Ferrer, G. Donati, R. Improta, N. Rega and F. Santoro, *J. Phys. Chem. A*, 2015, **119**, 5426–5438.

20 A. M. Alvertis, R. Pandya, L. A. Muscarella, N. Sawhney, M. Nguyen, B. Ehrler, A. Rao, R. H. Friend, A. W. Chin and B. Monserrat, *Phys. Rev. B*, 2020, **102**, 081122.

21 M. Schreiber, M. R. Silva-Junior, S. P. A. Sauer and W. Thiel, *J. Chem. Phys.*, 2008, **128**, 134110.

22 T. J. H. Hele, B. Monserrat and A. M. Alvertis, *J. Chem. Phys.*, 2021, **154**, 244109.

23 C. Simserides, A. Morphis and K. Lambropoulos, *J. Phys. Chem. C*, 2020, **124**, 12834–12849.

24 C. Simserides, A. Morphis and K. Lambropoulos, *Materials*, 2020, **13**, 3979.

25 P. Hohenberg and W. Kohn, *Phys. Rev.*, 1964, **136**, B864–B871.

26 W. Kohn and L. J. Sham, *Phys. Rev.*, 1965, **140**, A1133–A1138.

27 E. Runge and E. K. U. Gross, *Phys. Rev. Lett.*, 1984, **52**, 997–1000.

28 K. Lopata and N. Govind, *J. Chem. Theory Comput.*, 2011, **7**, 1344–1355.

29 E. Aprà, E. J. Bylaska, W. A. de Jong, N. Govind, K. Kowalski, T. P. Straatsma, M. Valiev, H. J. J. van Dam, Y. Alexeev, J. Anchell, V. Anisimov, F. W. Aquino, R. Atta-Fynn, J. Autschbach, N. P. Bauman, J. C. Becca, D. E. Bernholdt, K. Bhaskaran-Nair, S. Bogatko, P. Borowski, J. Boschen, J. Brabec, A. Bruner, E. Cauët, Y. Chen, G. N. Chuev, C. J. Cramer, J. Daily, M. J. O. Deegan, T. H. Dunning, M. Dupuis, K. G. Dyall, G. I. Fann, S. A. Fischer, A. Fonari, H. Früchtl, L. Gagliardi, J. Garza, N. Gawande, S. Ghosh, K. Glaesemann, A. W. Götz, J. Hammond, V. Helms, E. D. Hermes, K. Hirao, S. Hirata, M. Jacquelin, L. Jensen, B. G. Johnson, H. Jónsson, R. A. Kendall, M. Klemm, R. Kobayashi, V. Konkov, S. Krishnamoorthy, M. Krishnan, Z. Lin, R. D. Lins, R. J. Littlefield, A. J. Logsdail, K. Lopata, W. Ma, A. V. Marenich, J. Martin del Campo, D. Mejia-Rodriguez, J. E. Moore, J. M. Mullin, T. Nakajima, D. R. Nascimento, J. A. Nichols, P. J. Nichols, J. Nieplocha, A. Otero-de-la Roza, B. Palmer, A. Panyala, T. Pirojsirikul, B. Peng, R. Peverati, J. Pittner, L. Pollack, R. M. Richard, P. Sadayappan, G. C. Schatz, W. A. Shelton, D. W. Silverstein, D. M. A. Smith, T. A. Soares, D. Song, M. Swart, H. L. Taylor, G. S. Thomas, V. Tipparaju, D. G. Truhlar, K. Tsemekhman, T. Van Voorhis, A. Vázquez-Mayagoitia, P. Verma, O. Villa, A. Vishnu, K. D. Vogiatzis, D. Wang, J. H. Weare, M. J. Williamson, T. L. Windus, K. Woliński, A. T. Wong, Q. Wu, C. Yang, Q. Yu, M. Zacharias, Z. Zhang, Y. Zhao and R. J. Harrison, *J. Chem. Phys.*, 2020, **152**, 184102.

30 P. Löwdin, *J. Chem. Phys.*, 1950, **18**, 365–375.

31 T. H. Dunning, *J. Chem. Phys.*, 1989, **90**, 1007–1023.

32 W. J. Hehre, R. Ditchfield and J. A. Pople, *J. Chem. Phys.*, 1972, **56**, 2257–2261.

33 P. C. Hariharan and J. A. Pople, *Theor. Chim. Acta*, 1973, **28**, 213–222.

34 T. Torelli and L. Mitas, *Phys. Rev. Lett.*, 2000, **85**, 1702–1705.

35 Z. Liu, T. Lu and Q. Chen, *Carbon*, 2020, **165**, 468–475.

36 T. Lu, Z. Liu and Q. Chen, *Materials Science and Engineering: B*, 2021, **273**, 115425.

37 A. D. Becke, *The Journal of Chemical Physics*, 1993, **98**, 5648–5652.

38 C. Lee, W. Yang and R. G. Parr, *Phys. Rev. B*, 1988, **37**, 785–789.

39 S. H. Vosko, L. Wilk and M. Nusair, *Can. J. Phys*, 1980, **58**, 1200–1211.

40 P. J. Stephens, F. J. Devlin, C. F. Chabalowski and M. J. Frisch, *J. Phys. Chem.*, 1994, **98**, 11623–11627.

41 A. D. Becke, *Phys. Rev. A*, 1988, **38**, 3098–3100.

42 B. Monserrat, *J. Phys. Condens. Matter*, 2018, **30**, 083001.

43 F. Coppola, P. Cimino, U. Raucci, M. G. Chiariello, A. Petrone and N. Rega, *Chem. Sci.*, 2021, **12**, 8058–8072.

44 U. Raucci, F. Perrella, G. Donati, M. Zoppi, A. Petrone and N. Rega, *J. Comput. Chem.*, 2020, **41**, 2228–2239.

45 A. Petrone, G. Donati, P. Caruso and N. Rega, *J. Am. Chem. Soc.*, 2014, **136**, 14866–14874.

46 M. Rossi, P. Gasparotto and M. Ceriotti, *Phys. Rev. Lett.*, 2016, **117**, 1–6.

47 C. Haggard, V. G. Sadhasivam, G. Trenins and S. C. Althorpe, *J. Chem. Phys.*, 2021, **155**, 174120.

48 A. Petrone, D. B. Lingerfelt, D. B. Williams-Young and X. Li, *J. Phys. Chem. Lett.*, 2016, **7**, 4501–4508.

49 G. Donati, D. B. Lingerfelt, C. M. Aikens and X. Li, *J. Phys. Chem. C*, 2017, **121**, 15368–15374.

50 A. M. Alvertis, F. A. Schröder and A. W. Chin, *J. Chem. Phys.*, 2019, **151**, 084104.

51 R. Crespo-Otero and M. Barbatti, *Theor. Chem. Acc.*, 2012, **131**, 1–14.

52 S. Bai, R. Mansour, L. Stojanović, J. M. Toldo and M. Barbatti, *J. Mol. Model.*, 2020, **26**, 107.

53 W. L. Hase, R. J. Duchovic, X. Hu, A. Komornicki, K. F. Lim, D.-h. Lu, G. H. Peslherbe, K. N. Swamy, S. V. Linde, A. Varandas

and R. J. Wolf, *QCPE*, 1996, **16**, 671.

54 G. H. Peslherbe, H. Wang and W. L. Hase, in *Monte Carlo Methods in Chemical Physics*, ed. I. Prigogine and S. A. Rice, John Wiley & Sons, Ltd, 1999, vol. 105, ch. Monte Carlo Sampling for Classical Trajectory Simulations, pp. 171–201.

55 S. Hirata and M. Head-Gordon, *Chem. Phys. Lett.*, 1999, **314**, 291–299.

56 F. J. Ferrer, J. Cerezo, E. Stendardo, R. Improta and F. Santoro, *J. Chem. Theory Comput.*, 2013, **9**, 2072–2082.

57 S. Grimme, J. Antony, S. Ehrlich and H. Krieg, *J. Chem. Phys.*, 2010, **132**, 154104.

58 S. Arulmozhiraja and T. Ohno, *J. Chem. Phys.*, 2008, **128**, 114301.

59 F. Santoro, R. Improta, A. Lami, J. Bloino and V. Barone, *J. Chem. Phys.*, 2007, **126**, 084509.

60 H. Jónsson, G. Mills and K. W. Jacobsen, in *Classical and Quantum Dynamics in Condensed Phase Simulations*, ed. B. J. Berne, G. Ciccotti and D. F. Coker, World Scientific, 1998, ch. Nudged elastic band method for finding minimum energy paths of transitions, pp. 385–404.

61 G. Henkelman and H. Jónsson, *J. Chem. Phys.*, 2000, **113**, 9978–9985.

62 G. Henkelman, B. P. Uberuaga and H. Jónsson, *J. Chem. Phys.*, 2000, **113**, 9901–9904.

63 S. Smidstrup, A. Pedersen, K. Stokbro and H. Jónsson, *J. Chem. Phys.*, 2014, **140**, 214106.

64 L. Zhang, H. Li, Y. P. Feng and L. Shen, *J. Phys. Chem. Lett.*, 2020, **11**, 2611–2617.

65 L. Monacelli, I. Errea, M. Calandra and F. Mauri, *Nature Physics*, 2021, **17**, 63–67.